J Therm Spray Tech (2024) 33:652–665
https://doi.org/10.1007/s11666-024-01712-8

ORIGINAL RESEARCH ARTICLE

The Influence of Spraying Parameters and Powder Sizes on the Microstructure and Mechanical Behavior of Cold-Sprayed Inconel®625 Deposits

F. Taherkhani[1] · A. List[1] · S. Keller[2] · N. Kashaev[2] · F. Gärtner[1] · T. Klassen[1]

Submitted: 14 July 2023 / in revised form: 17 December 2023 / Accepted: 30 December 2023 / Published online: 1 February 2024

Abstract Cold spraying (CS) of high-strength materials, e.g., Inconel®625 is still challenging due to the limited material deformability and thus high critical velocities for achieving bonding. Further fine-tuning and optimization of cold spray process parameters are required, to reach higher particle impact velocities and temperatures, while avoiding nozzle clogging. Only then, sufficiently high amounts of well-bonded particle–substrate and particle–particle interfaces can be achieved, assuring high cohesive strength and minimum amounts of porosities. In this study, Inconel®625 powder was cold sprayed on carbon steel substrates, using N_2 as propellant gas under different spray parameter sets and different powder sizes for a systematic evaluation. Coating microstructure, porosity, electrical conductivity, hardness, cohesive strength, and residual stress were characterized in as-sprayed condition. Increasing the process gas temperature or pressure leads to low coating porosity of less than 1% and higher electrical conductivity. The as-sprayed coatings show microstructures with highly deformed particles. X-ray diffraction reveals that powder and deposits are present as γ-solid-solution phase without any precipitations. The deposits show high microhardness and compressive residual stresses, which is attributed to work hardening and peening effects. The optimized deposits reach almost bulk material properties and are thus well suited for industrial applications.

Keywords additive manufacturing · coating microstructure · cold spray · impact condition · Inconel®625 · mechanical properties · residual stress

This article is an invited paper selected from presentations at the 2023 International Thermal Spray Conference, held May 22-25, 2023, in Québec City, Canada, and has been expanded from the original presentation. The issue was organized by Giovanni Bolelli, University of Modena and Reggio Emilia (Lead Editor); Emine Bakan, Forschungszentrum Jülich GmbH; Partha Pratim Bandyopadhyay, Indian Institute of Technology, Karaghpur; Šárka Houdková, University of West Bohemia; Yuji Ichikawa, Tohoku University; Heli Koivuluoto, Tampere University; Yuk-Chiu Lau, General Electric Power (Retired); Hua Li, Ningbo Institute of Materials Technology and Engineering, CAS; Dheepa Srinivasan, Pratt & Whitney; and Filofteia-Laura Toma, Fraunhofer Institute for Material and Beam Technology.

✉ F. Taherkhani
farrokh.taherkhani@hsu-hh.de

[1] Institute of Materials Technology, Helmut-Schmidt-University/University of the Federal Armed Forces Hamburg, 22043 Hamburg, Germany

[2] Department of Laser Processing and Structural Assessment, Helmholtz-Zentrum Hereon, Institute of Materials Mechanics, 21502 Geesthacht, Germany

Introduction

In cold spraying (CS), feedstock powder is deposited onto substrates in solid state without melting. Particles are accelerated to supersonic speeds by high-pressure and high-temperature gas via a de-Laval nozzle (Ref 1-5). If the powder's velocities upon impact are above a material-dependent critical velocity, the transformation of kinetic energy into strain and thermal energy causes the material to undergo severe plastic deformation, leading to adiabatic shear instabilities (ASI). In this process, oxide scales are stretched and removed, and finally metallurgical bonding at the interface or already deposited layer occurs (Ref 2, 6-9). Any velocity in excess of the critical velocity, i.e., additional kinetic energy, will lead to a higher extent of ASI and more heat generation, increasing the well-bonded interface area and the tensile strength of the deposit.

Correspondingly, the coating quality parameter η, defined as the ratio of impact velocity (v_{imp}) to critical velocity (v_{crit}), has to exceed 1, and the bonded area between particle and substrate increases with increasing η. Typically, coating properties similar to those of bulk material are already achieved for η–values around 1.5 (Ref 10), while too high values of η could lead to hydrodynamic behavior and material loss.

CS of Inconel®625 has raised the interest of both the research community and industry. Inconel®625 is a nickel-based superalloy that is widely used as a coating in aerospace, energy, automobiles, maritime, chemistry, oil, and gas industries in order to improve wear and strength, enhancing surface properties of less expensive metallic components (Ref 1, 2, 7, 8). Due to its high molybdenum content, Inconel®625 is also a reasonable candidate for seawater applications, which suffer from higher risks of pitting and crevice corrosion (Ref 1).

Owing to the high strength and low deformability of the Inconel®625 powder in gas-atomized condition (Ref 10), and owing to the risk of nozzle clogging, the CS of this material is still challenging. Successful deposition of Inconel®625 coatings by CS has been previously reported (Ref 2, 11-14), which shows the potential of CS Inconel®625 for repair and surface enhancement. Since CS enables deposition under lower energy consumption than classic metal additive manufacturing processes such as Selective Laser Melting (SLM) and higher deposition rates of up to 14 kg/h (Ref 15), being about 3-times higher than under Wire Arc Additive Manufacturing (WAAM), this technique is an interesting alternative to conventional additive manufacturing methods. In this context, building structures like walls made up of high strength materials such as Inconel®625 by CS were reported (Ref 16). In other works (Ref 17, 18), CS was used to spray Inconel®625 to repair metal components. The resulting low porosity levels and high hardness values demonstrated the good quality of the cold-sprayed Inconel®625 coatings and showed that CS is a promising additive manufacturing technique for repair applications of Ni-based superalloy parts.

Most of the works have focused on microstructure evolution and mechanical properties of deposits. Some works investigated the effect of heat treatment on the residual stress of CS coatings and reported that residual stress in as sprayed state was not uniform and that heat treatments could induce tensile stress due to the elimination of porosities (Ref 1).

Wu et al. have deposited Inconel®625 coatings on 6061 aluminum alloy. The microstructure, mechanical and tribological properties of the coatings were systematically studied. The cold-sprayed Inconel®625 coatings had a low porosity level and EBSD analyses revealed that grain refinement occurred within the coatings and substrates could be attributed to strain accumulation and fragmentation process (Ref 2). Neo et al. studied the effect of different spray stand-off distance (SoD) on particle velocity of Inconel®625 during CS and reported that, there is an optimum SoD (8 mm) for given process parameter sets, which should ensure low porosity and high hardness given in this study (Ref 3). Some authors (Ref 19-21) have used different particle shapes of feedstock powder to demonstrate that changing of gas pressure and temperature greatly influences the particle velocity leading to less porous coatings. As well, it is argued that spherical and smaller particles provide better properties. Cavaliere et al. demonstrated that the hardening effect of the coating influenced the fretting behavior of the deposits using different particle dimensions (Ref 8). In another work, they described the fatigue behavior of Inconel®625 CS coatings and demonstrated that heat treatments have a beneficial effect on fatigue crack retardation (Ref 22). Azarmi et al. (Ref 23) investigated the elastic properties of Inconel®625 deposits that were cold gas sprayed onto aluminum substrate and concluded that the dislocation density at the grain boundaries is the major microstructural feature affecting the Young's modulus of cold sprayed coatings. Reported stress–strain tests indicated 30% reduction of the in-plane Young's modulus of the coating as compared to the bulk material. In another work, the inter-splat bonding fraction of the coatings sprayed (at the impacting interfaces of IN625 and IN718 in cold spraying) at different process conditions was estimated through FEM simulations based on the interface temperature and indicated an increase as a function of stagnation temperature (Ref 24).

Despite the works reported for CS of Inconel®625 so far, there is still a lack of understanding of the interplay between process parameters (temperature and pressure), powder size, and coating characteristics to achieve required deposit properties. Since the process gas pressure and temperature play a crucial role for the particle impact velocity (Ref 6, 10), the influence of the pressure and gas temperature on various properties of thick Inconel®625 deposits were addressed in detail in the present study with respect to the concept of coating quality parameter η.

Materials and Methods

Powder Analysis

Commercial Inconel®625 powder produced by Ar-gas atomization (PRAXAIR Surface Technologies, Indianapolis, Indiana, USA) of three different particle size distributions was used for cold spraying. The powder size distributions (PSD) and morphologies were analyzed by

laser diffraction (LA-910 Horiba, Kyoto, Japan) and by scanning electron microscopy (SEM, Quanta 650, FEI, Brno, Czech Republic) in SE (secondary electron) and EBSD (electron backscatter diffraction) modes, respectively. Structural analyses by x-ray diffraction (XRD) of the as-received powder were performed by using a D8 DISCOVER x-ray diffractometer from Bruker (Billerica, Massachusetts, USA). The chemical composition of the powder was measured by energy-dispersive x-ray spectroscopy (EDS) from FEI (Brno, Czech Republic), integrated into the used SEM. Single powder particle plastic behavior and the corresponding compression strength were determined by particle compression tests as described by Assadi et al. (Ref 25) using a modified micro-indenter from Zwick-Roell (Ulm, Germany) by applying a flat punch diamond tip of 200 µm diameter at a maximal load of 3 N.

Cold Spraying

Based on the experimentally measured UTS of the Inconel feedstock powder as input data, the KSS-software (Kinetic Spray Solutions GmbH, Buchholz, Germany) was used to define the cold spray process parameter sets, i.e., T_{gas} and P_{gas}, with respect to attainable η-values according to the well-known approaches from Schmidt et al. (Ref 26) and Assadi et al. (Ref 20). Corresponding particle impact conditions were calculated by considering the experimentally determined particle size distribution (PSD) of the received powder as well as physical data concerning density and specific heat of the feedstock material. Critical velocities were calculated on basis of experimental data on powder UTS and tabulated material data (melting temperatures, density, specific heat).

Cold spraying was performed by using an Impact Spray System 5/11 (Impact Innovations GmbH, Rattenkirchen, Germany) with a 100 mm pre-chamber length, corresponding to a powder injection at 128 mm upstream of the nozzle throat, and a commercial nozzle of type "SiC-OUT1" (Impact Innovations, Rattenkirchen, Germany) with an expansion ratio of 5.6 was employed. Nitrogen was used as propellant and as carrier gas. In order to correlate the corresponding particle impact conditions to attainable coating properties, the gas temperature (T_{gas}) and pressure (P_{gas}) were varied in a range from 800 to 1100 °C as well as from 40 to 50 bar, respectively. For the coarse and the fine powder sizes, only selected parameter sets were applied. Table 1 summarizes the cold spray conditions and calculated coating quality parameters (η) for the different mean particle sizes D_{50}.

The parameter set with T_{gas} = 1000 °C and P_{gas} = 50 bar was considered as reference condition (ref.) in this study. During primary parameter variation, the powder feed rate by disk rotation speed, the spray stand-off distance (SoD) and the line traverse gun speed were kept fixed at 2 rpm corresponding to 28.9 g/min (to prevent the particle collision & nozzle clogging), 20 mm and 250 mm/s, respectively. S235-structural steel substrates with dimensions of 70 mm × 50 mm × 3 mm were grit-blasted with #200 mesh alumina particles at room temperature by using a pressure of 6 bar and at an impact angle of 45° before starting the CS deposition. It should be noted that the deposition had to be interrupted every ten layers for grit blasting to clean the nozzle and to avoid nozzle clogging. For this, a second powder feeder loaded with Al_2O_3 with the trade name EK-180 (Wiwox, Erkrath, Germany) was used. Such refreshing of the nozzle was performed at a spray gun position sufficiently far away from the part in front of the exhaust system to avoid any influence on the already deposited material. The full deposits were processed as a sequence of 35 layers and built up in a minimum thickness of 1.9 mm to ensure dimensions that allow the machining of micro-flat tensile (MFT) test samples with 1 mm thickness.

Table 1 Calculated particle impact temperatures and velocities as well as η-values for applying different spray parameters to varied powder sizes

P, bar	T, °C	V_p, m/s	T_p, °C	V_{cr}, m/s	D_{50}, µm	η
50	800	618	559	667	33-middle	0.95
50	900	673	638	630	33-middle	1.02
50	**1000**	**655**	**717**	**591**	**33-middle**	**1.11**
50	1100	672	796	549	33-middle	1.22
40	900	614	643	628	33-middle	0.99
40	1000	630	722	598	33-middle	1.07
50	**1000**	**694**	**650**	**656**	**25-fine**	**1.06**
50	**1000**	**605**	**769**	**532**	**45-coarse**	**1.14**
50	1100	618	852	488	45-coarse	1.27

Bold values illustrate significant changing parameter during this study

Characterization Methods

The electrical conductivity measurements of deposits (σ_E) were carried out according to the ASTM-Standard E1004 on grinded-surface samples (finish with 1000 SiC grit size) by using a Sigmascope SMP10-HF device and an ES40HF sensor (Helmut Fischer, Sindelfingen, Germany). A coating thickness of > 1 mm and a frequency of 1250 kHz should ensure that influences from the substrates are avoided.

For preparing coating cross sections, deposited samples were hot mounted in a conductive resin and polished using standard metallographic techniques down to OPS (oxide polishing suspension, 0.05 µm) as the final finish. Coating microstructures were analyzed by using an optical microscope (OM) of type DMRM (Leica, Germany) with the Axion-Vision analysis software and a scanning electron microscope of type Quanta 650 (FEI, Brno, Czech Republic).

Microhardness was measured in through-thickness locations on the polished cross section using a universal hardness testing machine of type ZHU0.2 (Zwick/Roell Instruments, Germany) at room temperature with Vickers indenter under a load of 2.95 N ($HV_{0.3}$), using a dwell time of 10 sec. Data on the crystallographic structure of the as-sprayed samples were obtained by x-ray diffraction (XRD) by using an instrument of type D8 DISCOVER Bruker (Massachusetts, USA) and applying Cu-k_α radiation. Micro-strain and lattice parameters were calculated with TOPAS-64-V6 from Bruker, which is a fitting-based software for crystal analysis.

The residual stress analyses of the coatings were determined by the incremental hole-drilling method using a PRISM system from Stresstech (Rennerod, Germany), which is based on electronic speckle pattern interferometry (ESPI) that provides high-quality full-field displacement data for accurate residual stress calculation. For all performed measurements, holes of 2 mm in diameter and 1 mm in depth were drilled incrementally. Four determined residual stress measurements were averaged to have sufficient statistics.

Micro-flat-tensile (MFT) tests were performed in order to determine mechanical properties of the deposits. For the preparation of MFT test samples, the deposit material was sprayed onto flat substrates and cut into desired test sample geometries (L × W × H: 30 × 5 × 1 mm; gauge length 9 mm) by electro-discharge erosion by setting the gauge direction and thus later the applied force parallel to the spray lines. Details of the specimen geometry (Fig. 1a) as well as an overview image of one of the Inconel®625 samples after testing (Fig. 1b) are shown in Fig. 1. In deviation to the standard for tensile testing, the experiments were performed using a load-controlled procedure with a fixed strain rate of 0.25×10^{-3} 1/s and were carried out on a 5-kN electro-mechanic universal testing machine of type Z100 (Zwick/Roell, Ulm, Germany) at an increasing force rate of 2 N/sec till the complete fracture of the sample. The strain and elongation were optically recorded by a CCD camera of type videoXtens and analyzed by the commercially available software testXpert, both from Zwick/Roell (Ulm, Germany).

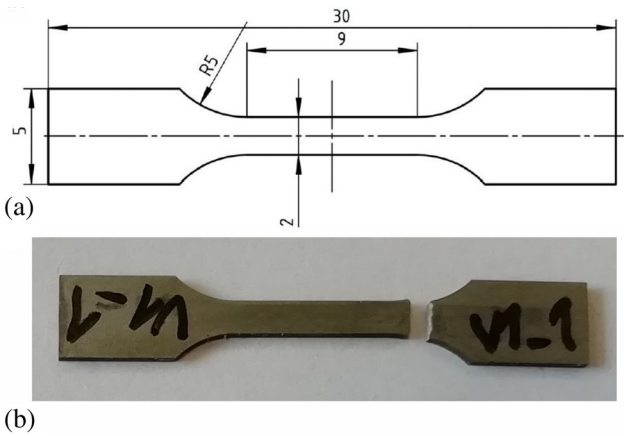

Fig. 1 Dimensions and geometry of the MFT samples according to DIN EN ISO 6892-1 with 1 mm thickness (a), and macro-view of the Inconel®625 sample after testing (b)

Results

Powder Microstructures and Properties

Morphologies and particle size distribution (PSD) of the as-received Inconel®625 medium-size powder as obtained from SEM and optical microscopy (OM) are presented in Fig. 2. Well separated spherical morphology with some small satellite particles is shown in Fig. 2(a). The PSD shows a maximum population at 32 µm and displays a unimodal and narrow distribution with d_{10} = 28 µm, d_{50} = 33 µm, and d_{90} = 38 µm, without undesired fine

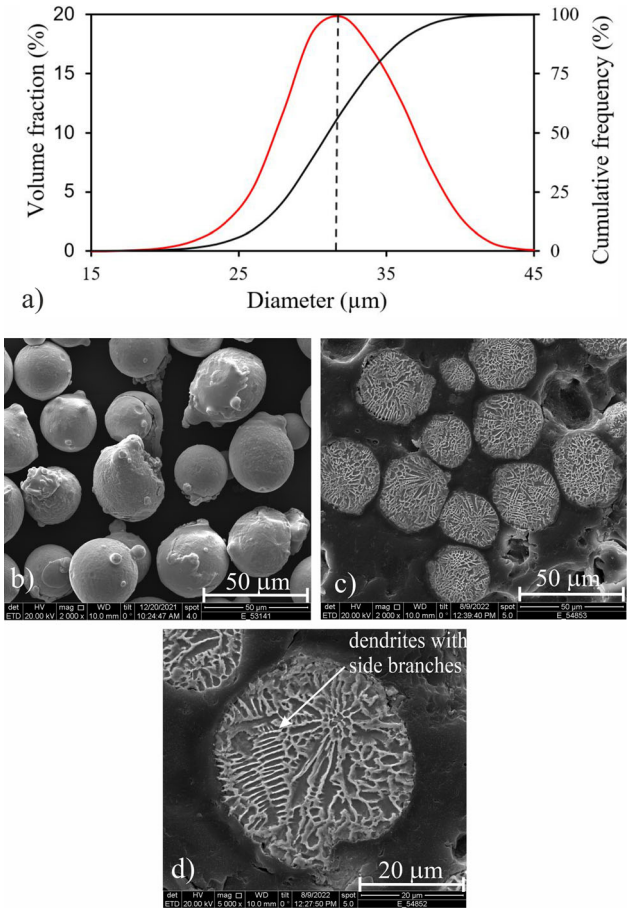

Fig. 2 Particle size distributions (a) and typical SEM- and OM-micrographs of the Inconel®625 powder feedstock showing the morphology (b), (c), (d)

fractions (<10 µm) (Fig. 2a-b). Micrographs of powder cross sections in Fig. 2(c)-(d) reveal cellular dendrites with side branches due to the high undercooling during rapid solidification in the gas atomization process. Nb segregation in interdendritic (gray) regions was confirmed by EDS.

In order to compare the influence of the powder size on the coating's properties, two additional powder batches, denoted as fine and coarse powder, from the same producer were used with PSDs of − 29 + 20 µm and − 53 + 41 µm, respectively.

Figure 3 shows the results of the experimentally determined UTS values for the different powder sizes. The results indicate a decrease of the UTS with increasing particle sizes.

According to the results from individual particles compression tests, the as-received powder has a mean UTS of 1512 ± 122 MPa, which is about 55% higher than that of soft-annealed Inconel®625 bulk material (957 MPa) (Ref 27).

Coating Microstructures

Typical cross section micrographs of as-sprayed deposits are shown in Fig. 4. Deposits are dense with rather low porosity (less than 2%), without cracking or delamination at the interface to the substrate. As illustrated in Fig. 4, the size and amount of porosities and micro-cracks are inversely proportional to the increasing η-value associated with increased process gas temperature (Fig. 4a-f).

According to Fig. 4(g)-(h), basic features of the powder microstructures after etching the polished-cross-section, such as dendritic or grain refined areas, were also observed inside the deformed particles. However, they are mostly elongated due to the particle deformation, as shown in Fig. 4(g). According to that, the overall particle deformation is rather high, despite of the high mechanical strength of the as-received powder. As observable in Fig. 4(h), close

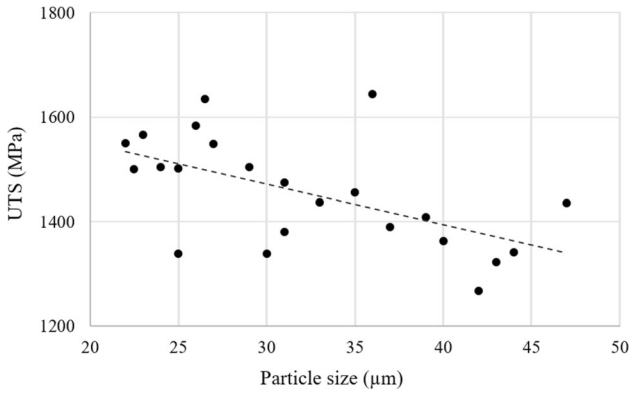

Fig. 3 Experimentally determined UTS values of the used Inconel®625 as a function of particle size

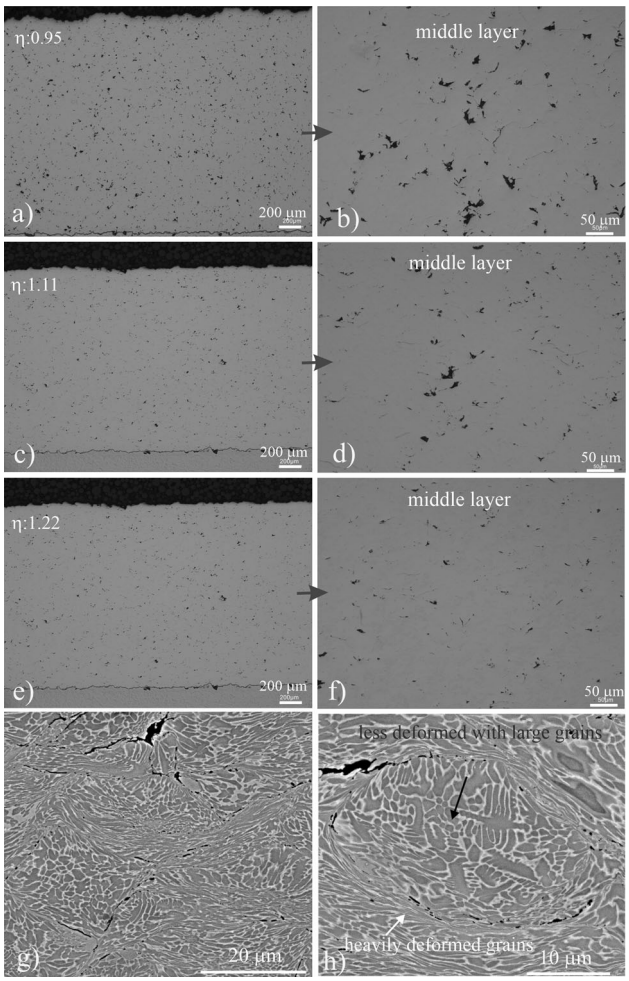

Fig. 4 Optical (left column) and SEM (right column) cross-sectional micrographs of cold-sprayed Inconel®625 deposits in the as-sprayed condition, using a gas temperature of 800 °C (a), 1000 °C (c) for the reference coating, and 1100 °C (e), as well as middle sections of the coatings at higher magnification (b), (d), (f). Etched cross sections of the ref. coating are shown in (g) and in (h) at higher magnification, which indicate particle boundaries (g) and the deformed particle (h)

to interparticle boundaries, highly elongated grains are observed by locally obtained high degrees of deformation. According to this figure, the microstructure of a deformed particle comprises highly deformed regions and less deformed ones, corresponding to peripheral and interior regions of the particle, respectively. These micrographs also reveal the presence of some pores and non-bonded interfaces located at the particle–particle interfaces.

Figure 5 compares the middle section of the deposits, as produced using different powder sizes and the reference spray parameter set. These micrographs reveal that the size of the micro-porosities tends to be larger with increasing the powder size. Figure 5(d) and (e) shows etched microstructures for coatings on basis of the coarse powder size in order to reveal microstructural feature with respect to particle deformability (compare Fig. 4g and h). In the

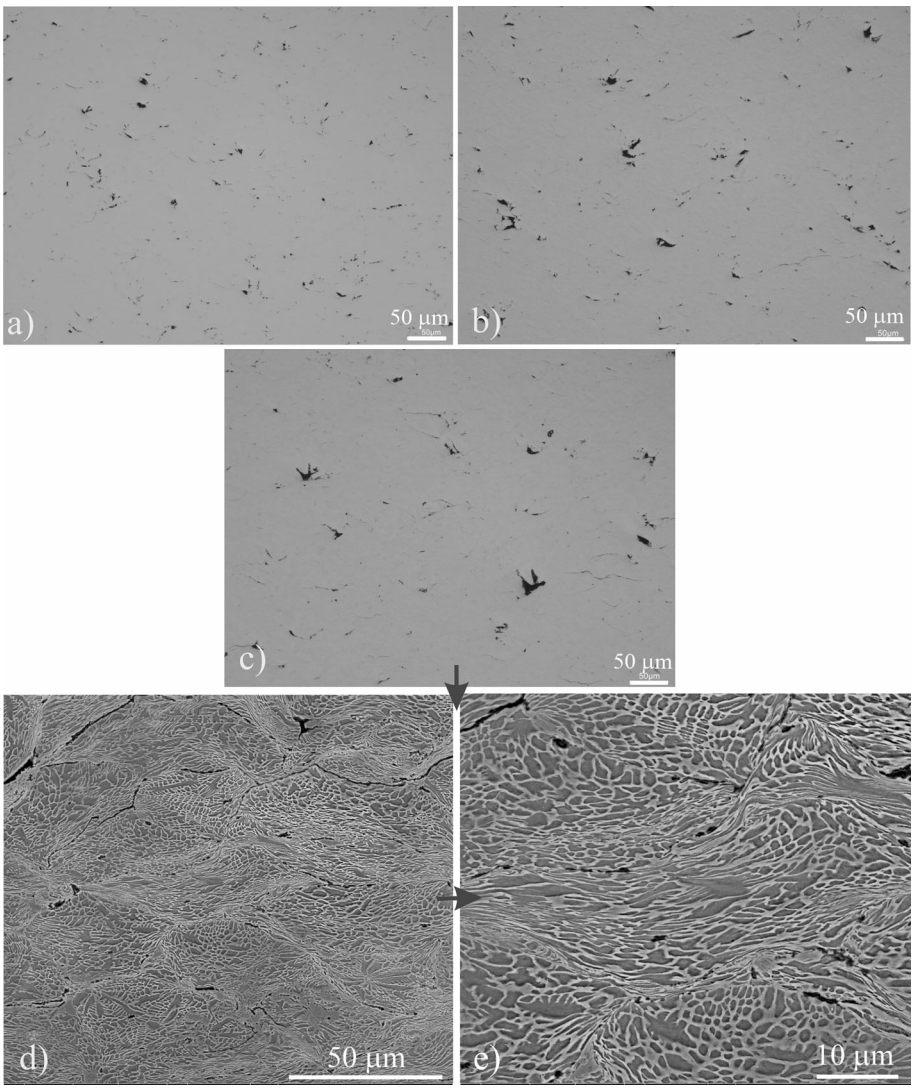

Fig. 5 Optical and SEM cross-sectional micrographs of cold-sprayed Inconel®625 deposits in the as-sprayed condition by using the ref. parameter set using 1000 °C and 50 bar for fine (a), medium (b), and coarse (c) powder sizes. An etched cross section of the deposit on base of the coarse powder is shown at higher magnification in (d) and (e), which indicate particle boundaries (d) and the deformed particles (e)

case of the coarse powder (Fig. 5d, e), particle deformation appears as more homogeneous, resulting in more rather uniform microstructure than within the coatings on basis of the medium size (Fig. 4g, h). Moreover, it can be seen that the deformation gradient from the interior region of the deformed particle toward the peripheral area (Fig. 5e) is less than that of the medium powder (Fig. 4h).

Figure 6 compares the XRD patterns of the as-sprayed reference sample and the as-received Inconel®625 powder. Eight peaks were identified that correspond to (111), (200), (220), (311), (222), (400), (331), (420) lattice planes, which are characteristic of the solid solution fcc γ-phase. The XRD pattern of the as-received powder shows peak-asymmetries and already large Full Widths at Half Maximum (FWHM). This could be due to the micro-segregation in the interdendritic region of primary dendrites as obtained under the high solidification rate in the gas atomizing process.

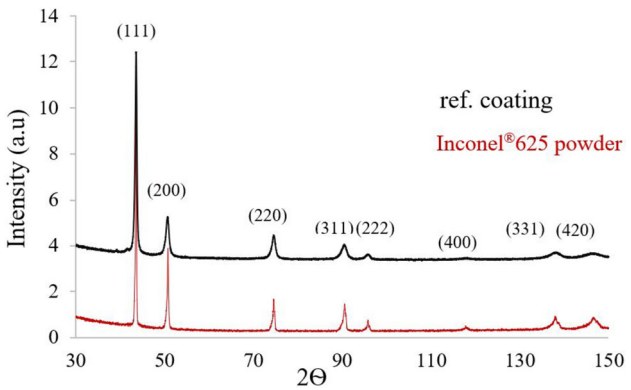

Fig. 6 XRD pattern of the Inconel®625 feedstock powder as well as the reference coating

In comparison with that of the initial powder, the XRD pattern of the reference deposit shows broader peaks with larger FWHM. This can be explained by additional elastic

strains due to strain hardening and high dislocation densities, here being recorded as crystal defects. The peak-asymmetries of the initial powder are retained in the structures of the as-sprayed reference coating. The asymmetry can be interpreted as superimposed effect, here grains with different chemical composition and thus different lattice constant. Hence, in order to represent the matrix and the partitioning effects, two separate phases were detected and considered by TOPAS software during the analysis of XRD data of powder and deposit. Using TOPAS software, microstrains were calculated for the two phases. The results reveal microstrains of 0.562×10^{-3} and 1.920×10^{-3} within phases 1 (matrix) and 2 (partitioning) of the as-received powder. Within the reference coating, microstrains are higher with 1.78×10^{-3} (phase 1, matrix) and 3.86×10^{-3}, (phase 2, partitioning), indicating the increase in dislocation density by work hardening.3.3 Coating Properties

With respect to coating properties, correlations between data of calculated coating quality parameters η attained under different process conditions and obtained porosities, electrical conductivities, cohesive strengths (UTS), micro-hardness (HV0.3), and residual stresses are illustrated in Fig. 7, 8, 9, 10, 11, 12.

Figure 7 shows the average electrical conductivity and reveals a direct correlation with the η-values, for high-end conditions approaching the bulk reference value. However, the comparison to hot rolled material should be treated with care. Dynamic recrystallization during the hot rolling and formation of carbides, γ' precipitations and δ phases could contribute to electron scattering and reduced electron mobility, and thus comparatively low electrical conductivity (Ref 28, 29). In consequence, the bulk conductivity can be reached and may be even surpassed in case of CS deposits. Such is reached by using the finer powders already at rather low η-values. The difference in conductivities between coatings on basis of fine and coarser powders could be attributed to local defect densities and

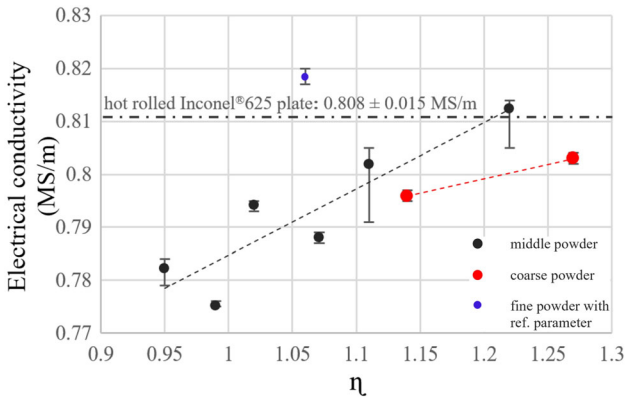

Fig. 7 Correlation between electrical conductivities and η-values

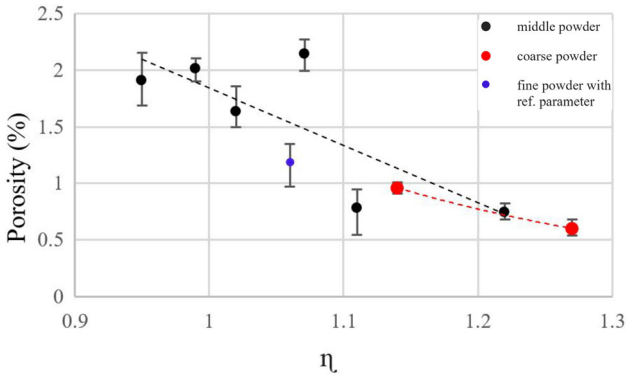

Fig. 8 Correlation between deposit porosities (%) and η-values for using different powder feedstock sizes

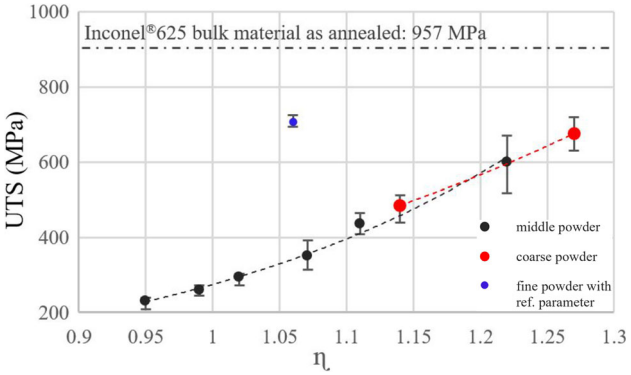

Fig. 9 Correlation between UTS and η-values attained in CS of Inconel®625 powder

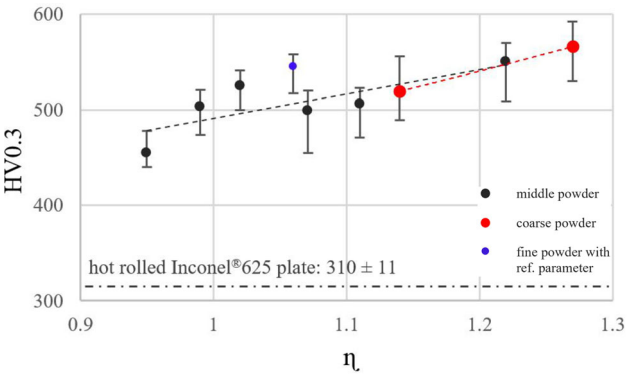

Fig. 10 Correlation between micro-hardness and η-values

amounts of well-bonded internal interfaces. However, also different amounts of regions that are subject to dynamic recrystallization and thus fewer scattering centers must be considered.

The mean deposit porosities by using different powder feedstock sizes are illustrated in Fig. 8 and demonstrate a steady decrease with increasing η. For $\eta > 1.1$, porosities of less than 1% are reached. The decrease in porosity with increasing impact conditions by means of particle velocity

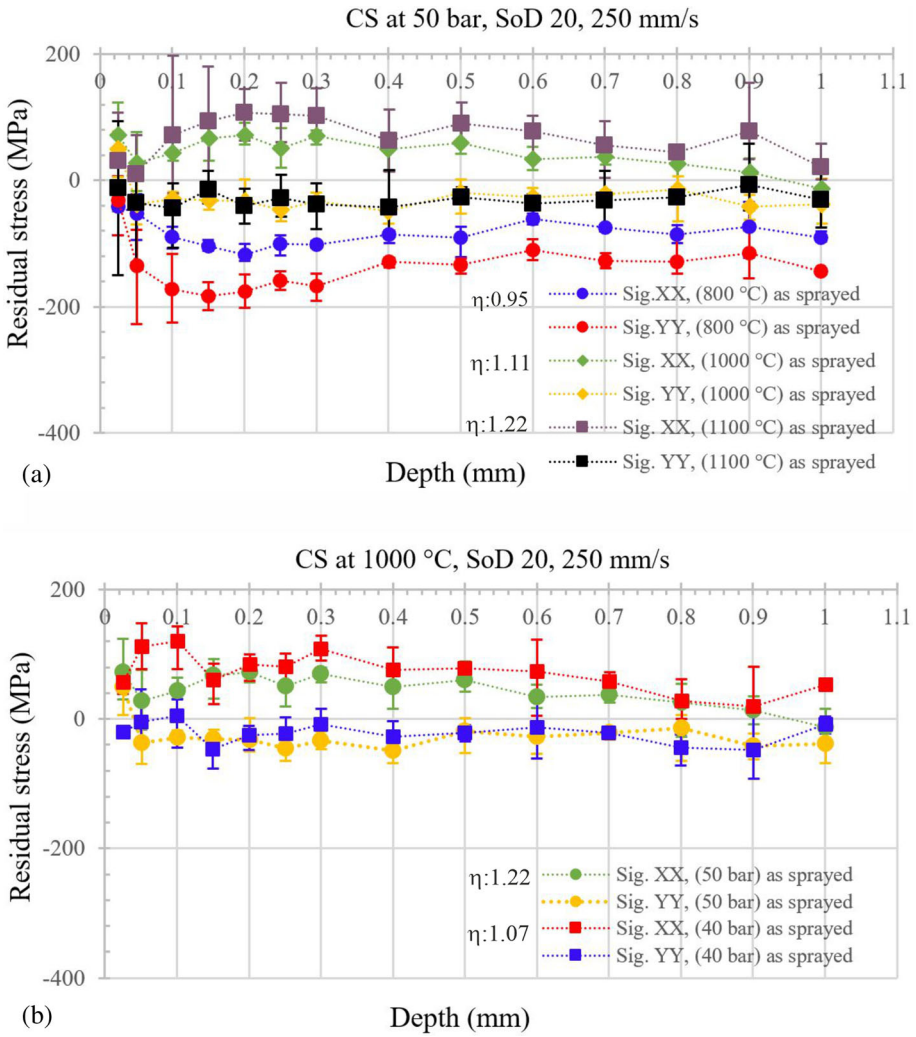

Fig. 11 Residual stress profile measured using the hole drilling method for the sprayed specimen at different (a) temperatures, (b) pressures

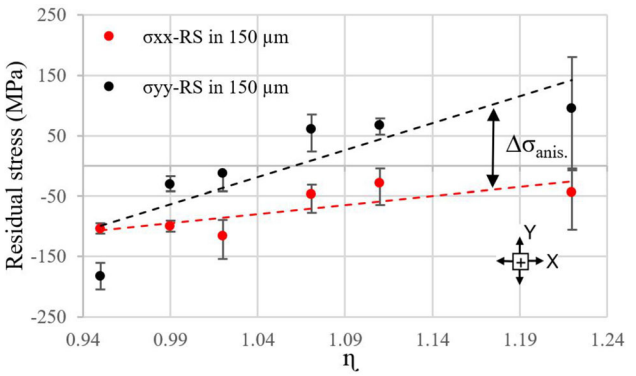

Fig. 12 Correlation between residual stresses within a depth of 150 µm for different η-values. The inserted arrow indicates the stress anisotropy (CS direction: Y)

and temperature can be explained by attained larger amounts of deformation and overall strain, ensuring better adoption to local surface topographies.

Figure 9 shows the experimentally determined coating strengths for different process conditions. For deposits on basis of the medium and coarse size powders, the data demonstrate that the average UTS directly scales with the η-values. Interestingly, the UTS of the material deposited with the fine powder does not fall onto the line. At same η, the recorded UTS is much higher than the one from the deposits sprayed with the other two powder batches (at the reference parameter set, η is even higher for the coarser powders). The maximum UTS of approximately 700 MPa corresponds to about 58% of the strengths given in wrought bulk material (approx. 1200, 957 MPa for annealed Inconel®625 (Ref 27)).

Figure 10 summarizes the obtained mean hardness data. The microhardness of the deposits tends to increase slightly with increasing η. In accordance with literature, this might just reflect the trend of decreasing porosities (Ref 30) as already shown in Fig. 8. The higher amount of porosity is due to the lower amounts of induced plastic deformation of

particles at lower η-values. Less work hardening in addition causes lower microhardness of the coatings.

Figure 11(a) and (b) illustrates the results on residual stress measurements obtained using the hole drilling technique. The measurements were performed at 4 locations in the middle of the sprayed area. By using a tool diameter of 2.0 mm, it was possible to obtain the residual stress profiles up to half deposit depth (1 mm). The obtained results depict a non-uniform depth-resolved residual stress profile, where the residual stresses σ_{xx} along the CS line direction are slightly higher than the residual stresses in the *y*-direction, σ_{yy}. The sprayed specimens at different temperature indicate that highest compressive and tensile residual stresses are obtained at depths of approximately 0.15 and 0.2 mm, respectively (Fig. 11a). It should be noted that the highest values of the obtained tensile and compressive residual stresses of approximately + 60 and − 200 MPa are smaller than the yield strength of the as-annealed bulk material (460 MPa) (Ref 27). It can be seen that the state of the residual stress changes with changing the process gas temperature. Nevertheless, changing the pressure does not influence the trend of generated residual stresses (Fig. 11b).

Since the residual stress profiles, apart from surface effects, show almost no significant gradients over deposit thickness, conditions at one defined depth from surface can be used for a more general comparison. Figure 12 shows the development of residual stresses with η-values at a depth of 150 µm below the top surface. The stresses are recorded parallel (y-direction) and perpendicular (X-direction) to the spray lines in cold spraying. At low η-values, compressive residual stresses are obtained for both directions. With increasing η, the absolute values of compressive stress decrease and even show transitions toward tensile stress conditions. However, due to the different slopes of the stress development for the two directions, the transition to tensile stresses is obtained at individually different η-values.

The differences between the two components of residual stresses σ_{xx} and σ_{yy} in Fig. 12 give clear evidence for residual stress anisotropies ($\Delta\sigma_{anisotropy} = \sigma_{xx}$-$\sigma_{yy}$). These stress anisotropies increase with higher η values, which are here associated with a higher degree of deformation but also higher deposit temperatures.

Coating Fractography

Figure 13 summarizes the OM (a, b) and SEM images (c, d, e) of fractured surfaces of the reference deposit after MFT testing (medium size powder, CS with 50 bar, 1000 °C). According to Fig. 13(a) and (b), deposit failure is dominated by growth of one main crack (white arrow). However, details of the cross section could reveal the presence of a secondary crack (red arrow) that finally did not lead to failure. The waviness of the fracture surface corresponds to the dimensions and shapes of splats within the coating, thus reflecting the internal microstructure and respective defects. This indicates that the crack growth direction mainly follows the splat interfaces.

Figure 13(c), (d) and (e) shows details of the fracture surface in top view and allow to distinguish between ductile and brittle features. According to the overview in Fig. 13(c), more than half of the fracture surface has a smooth topography, which more or less captures the shapes of individual spray splats of the deposit. These smooth areas are surrounded by rather rough topographies with individually different plastic deformation features ranging from dimples by ductile failure to rupture of barely deformed (strain hardened) areas.

The prevalent brittle behavior with a strain to failure of about 0.8% and limited traces of plastic deformation during the test could be explained by crack nucleation at defects, such as porosities and non-bonded interfaces, and respective growth and bridging to next potential crack nuclei. More details on the nature of failure can be derived from Fig. 13(d), (e), allowing to distinguish between low deformability rupture and ductile dimple failure.

Influences by spray conditions and, respectively, obtained deposit strengths on fracture topographies are captured in Fig. 14 by comparing coatings of different quality and strength according to the lowest the highest η from the range of this study. The comparison shows that the amount of dimple features increases with the η-value, indicating trends of changing fracture modes from brittle to brittle-ductile. Smooth splats and cleavage can be prominently seen on the fracture surface of the deposit processed here with lowest η (= 0.95). On the contrary ductile dimple or low deformability rupture features cover more than half of the fracture surface for the deposit manufactured with largest η (= 1.27).

Discussion

Due to the gas atomized nature and production conditions of the Inconel®625 powder, the structure revealed the presence of a solid solution and a supersaturated *Y*-phase with micro-segregation of Nb and Mo within interdendritic regions. The fine dendritic and cellular (refined) microstructure observed in Fig. 2(a) and (c) results in an about 50% higher UTS as compared to values of annealed bulk material. As a result, v_{crit} is higher, and impact conditions are not sufficient to reach the $\eta > 1.5$ regime as needed for obtaining bulk like properties within the deposits (Ref 31). In consequence, the extent of ASI and associated well-bonded areas with excellent particle–particle and particle–substrate bonding are lower than expected by estimations on basis of bulk property data.

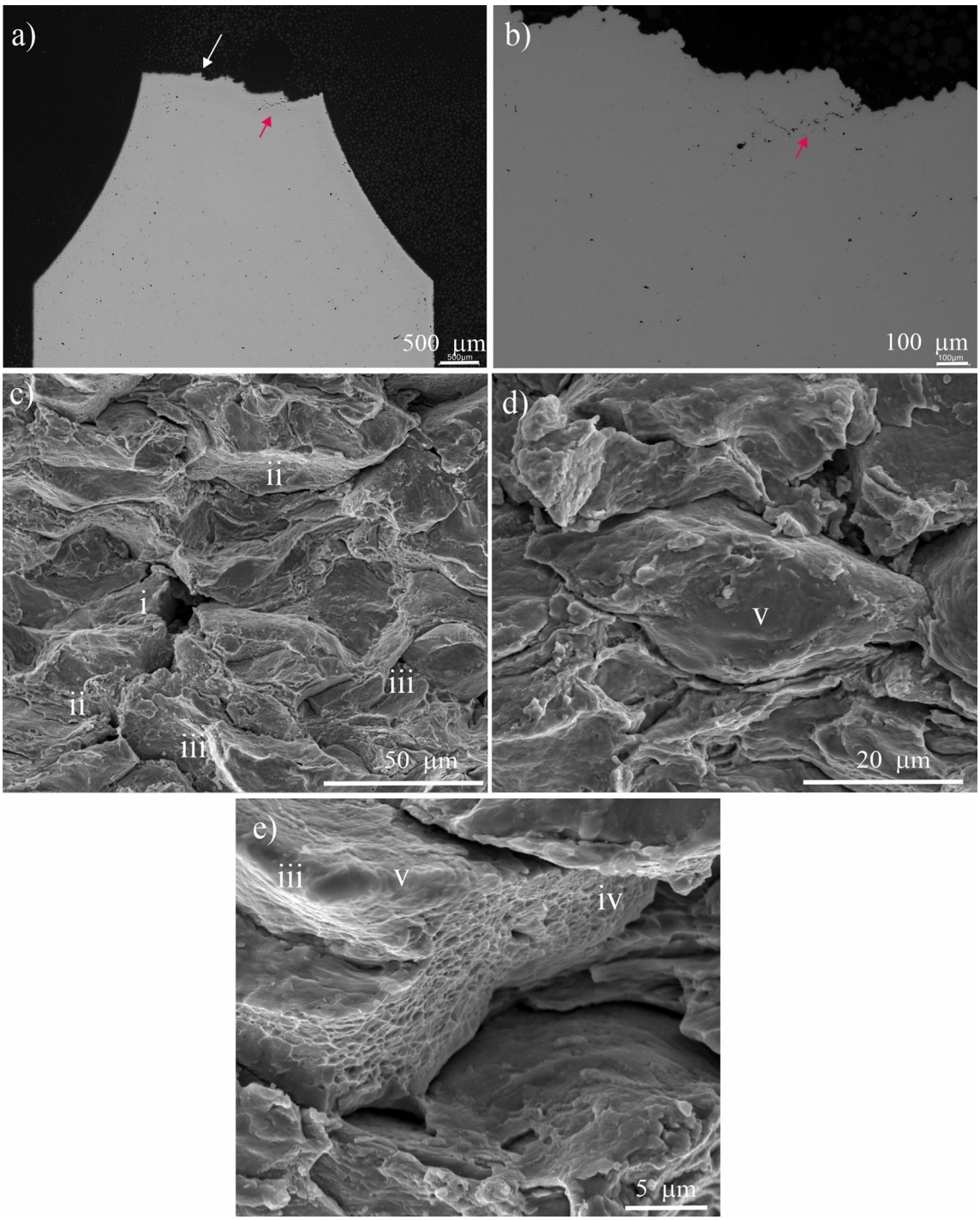

Fig. 13 Fractography analysis of the as-sprayed reference coating with OM micrographs of cross section in (a) and (b) and detailed top view SEM analyses of surface topographies in (c), (d) and (e). The inserts describe white arrow: main crack, red arrow: secondary crack, (i): porosity, (ii): non-bonded interface, (iii): highly deformed area with fine microstructure, (iv): dimples after fracture, (v): smooth splat with limited deformation

Furthermore, micro-defects in the coating are more likely to occur.

The dependence of UTS over particle size (Fig. 3) can be explained by the higher cooling rates of smaller particles and thus higher undercooling during solidification (Ref 25). According to the Hall–Petch relation, attained smaller internal grain sizes could be a major reason for the higher powder strengths, in addition to the partitioning during dendrite growth.

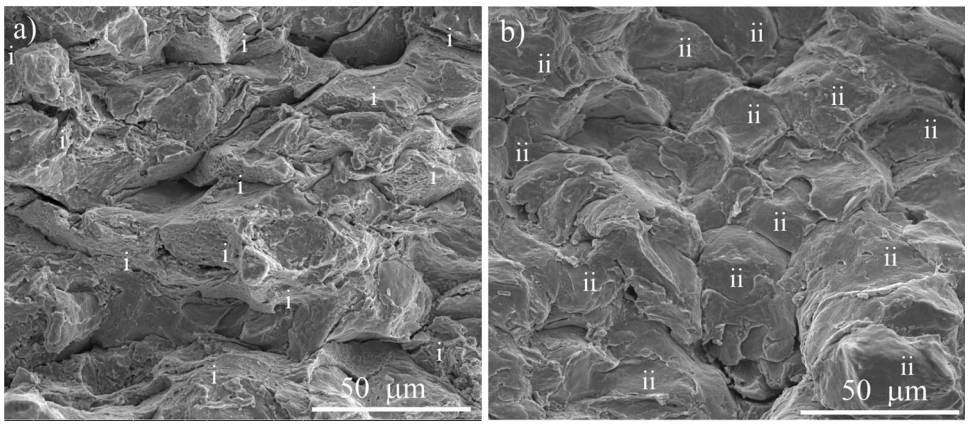

Fig. 14 Fracture surfaces of the as-sprayed coatings after failure in MFT testing; (a) for the largest η: 1.27, (b) for the smallest η: 0.95. The inserts describe (i): dimples, (ii): smooth splat with limited deformation

As given in Fig. 4, all deposits are rather dense with porosities less than about 2%. This is attributed to sufficient plastic deformation during CS, as visualized in Fig. 4(g). Overall high degrees of deformation allow to adopt to local topographies as observed for powder compaction (Ref 32). Associated local metallurgical bonding is caused by occurring adiabatic shear instabilities (ASI) under high strain rates and thermal softening. However, the high velocity impact during CS also introduces a variety of microstructural features that influence deposit properties. The particles experience large strains and strain rates during impact condition, that lead to work hardening in the vicinity of ASI. Due to the severe plastic deformation and the associated temperature rise, dynamic recovery and dynamic recrystallization may take place and can cause grain-refined regions (Fig. 4h) (Ref 21). Microstructures with bimodal grain sizes in CS deposits, as shown in Fig. 4(h), are therefore attributed to heterogeneous deformation strain and local temperatures showing steep gradients from the contact areas toward the interior regions of the spray splats (Ref 33). It may be assumed that the volume fraction of smaller crystallites is lower than that of coarser crystallites. This may lead to a systematic overestimation of average grain size and some underestimation of microstrain in evaluation of peak broadening in XRD by full width at half maximum of the peaks. Nevertheless, the deposits show larger micro-strains than the as-received powder, in agreement to literature, indicating increased defect densities due to deformation (Ref 14).

As indicated in Fig. 4(a), (c) and (e), impact of the first layer of particles causes more plastic deformation to the much softer S235 substrate, generating an interface with deep craters on substrate sides with less deformation by particles than found within the coating. Similar statement is given in literature (Ref 21). Differences in coating microstructures could be derived from the η-concept. In agreement to reported data (Ref 22), higher process gas temperatures should lead to reduced amounts of porosity due to the increase the particle deformation as showed in Fig. 4(a)-(f).

As considered in the η-concept, particle sizes could have several influences on deposit properties. On the one hand, the critical velocity is roughly decreasing with increase powder sizes. On the other hand, smaller particles by their smaller mechanical and thermal momentum reach higher velocities but lower temperatures than larger ones. However, in addition local temperature distributions could play a role for interface deformation. The cooling rate of the particle in the free jet decreases with increasing the powder size due to lower surface-to-volume ratios (Ref 21).

As illustrated in Fig. 7, 8, 9, 10, electrical conductivity, residual porosity, cohesive strength (UTS), and microhardness tend to improve with increasing η. This indicates that the η-concept can be used to predict and estimate the quality of cold-sprayed Inconel®625 deposits. According to the proposed equation to calculate v_{crit} (Ref 34, 35), increasing T_{gas} decreases v_{crit} and subsequently increases η as the ratio between v_{imp} and v_{crit}. In addition, particle velocity increases as T_{gas} and/or P_{gas} increase. As a result, the ability of a particle to undergo plastic deformation as well as flattening during impact is directly related to η. Furthermore, the fraction of non-bonded interfaces is reduced under higher impact conditions (Ref 36). Since the type of analyses not distinguishes whether internal interfaces are just compressed or metallurgically bonded, the increase in HV0.3 is mainly attributed to lower porosities attained by CS at higher η values.

The above descriptions hold well for the medium and coarse size powders. However, in case of the fine feedstock powder, obtained properties with respect to conductivity and UTS of deposits are better than predicted. This may be attributed to higher impact velocity and kinetic energy attained by smaller particles, which might play a more important role for bonding than the higher temperatures of larger ones. The topic of finding respective descriptions by considering individual size dependent deformation features

and deposit fracture mechanics is currently under investigation. In view of impact velocities and kinetic energies dominating ASI formation, the higher UTS as well as higher electrical conductivity of the deposits produced at reference conditions using the fine powder can probably be attributed to the higher extent of well-bonded interfaces. In addition, smaller micro-pore sizes and thus potential crack nuclei sites could contribute to lower stress concentration and better fracture toughness. Despite of the higher UTS of deposits processed with the fine powders, Fig. 9 shows that all coatings show lower UTS than the bulk material. The maximum obtained UTS of as-sprayed coatings is 26% lower than that reported for as-annealed Inconel®625 plates. Neglecting work hardening effects, this means that minimum one-fourth of internal particle interfaces was not bonded. In order to reach bulk like properties, post-treatments are needed to in order to reduce the number and sizes of non-bonded interfaces. Respective results are topic of current studies and an up-coming publication.

By the nature of impact, obtained stress states in cold spraying are so far mainly considered as compressive, similar to those reached by shot peening (Ref 37). This comparison holds as long as secondary influences are negligible. The results of deposit residual stresses from Fig. 12 indicate that the intrinsically compressive peening stresses of the cold-sprayed Inconel®625 deposits are superimposed by tensile contributions. The superimposed tensile stresses could be attributed to temperature gradients within the deposit. Accordingly, higher local temperatures and thus steeper gradients under the spray spot due to higher parameter sets and corresponding η values would result in more tensile stress contributions, in accordance with literature (Ref 1, 38). Apart from that, the temperature gradients also depend on local cooling rates under the heat input of the gas jet and impinging particles.

Particularly the heating and cooling conditions and associated temperature gradients could help to explain the observed stress anisotropies between parallel and perpendicular directions to the spray line trajectories. In order to supply more information on temperature distributions during the cold spray process, thermocouples were placed in different positions within the substrate close to surface. Respective results demonstrated that temperature gradients inline to the trajectory direction are lower than in vertical direction to the scanning line. Thus, higher surface temperatures and associated differences in thermal shrinkage and tensile contributions may explain the stress anisotropy in x- and y-direction for larger η values.

The fracture surface of the as-sprayed reference coating given in Fig. 13 shows a high amount of smooth areas due to de-cohesive fracture and scarce appearance of dimple features, thus explaining the brittle failure behavior at a strain to failure of 0.8% and limited traces of plastic deformation. Fracture mainly occurs at inter-particle boundaries, with only few traces of trans-splat or ductile dimple failure at well-bonded interfaces. The brittleness of the deposit is thus due to weak inter-splat bonding. The cold spray parameter sets determine the spread of metallurgical bonded areas by ASI and thus determine the proportion where ductile dimple features could be observed in tensile part failure. As given in Fig. 14, the amount of dimple features indicating well-bonded splats increases with increasing η-value. Higher amounts of well bonded ductile areas within the interfaces then determine the overall deformation behavior (Ref 31, 38) and thus deposit strength. However, potential growth of crack nuclei at non-bonded interfaces then also depends on local deformation behavior, work hardening and microstructures along the splat boundaries.

Conclusions

This study demonstrates the influence of cold spray parameters and powder sizes on the microstructure and mechanical behavior of thick cold-sprayed Inconel®625 deposits. First, it can be summarized that cold spraying of Inconel®625 at high parameter sets and η-values leads to dense deposits with close to bulk properties. No phase transformations and no oxidation are observed in the cold-sprayed deposits. Porosities were below 2% and could be reduced to less than 1%. Electrical conductivity, porosity, ultimate tensile strength, and microhardness show a good correlation with the calculated η-values and, respectively, increased cold spray parameter sets. The microstructure and homogeneity of particle deformation depend on particle size. An increase in UTS and decrease in porosity are due to larger fraction of well-bonded areas and can be influenced by the particle size, as well. At same parameter sets, the use of fine powder proves advantages for reaching a higher UTS of the deposit than attainable by using coarser sizes. The differences are attributed to better inter-particle bonding. Residual stresses are dominantly compressive, but superimposed by tensile contributions that increase with impact conditions and other influences on temperature gradients and thermal history. The obtained residual stress anisotropies are here mainly attributed to temperature gradients and higher maximum surface temperatures under increased the η-parameters. The failure mode of the fractured deposits is mainly brittle. Nevertheless, the amounts of well-bonded splats as well as dimple features increase with the η-values. It can be assumed that respective heat treatments could reduce amounts of non-bonded interfaces by recrystallization restore properties of respective material. Thus, in summary,

cold spraying appears as suitable for fabricating coatings as well as thicker deposits of Inconel®625.

Acknowledgments Support by T. Betschinski and T. Soehl from the Hartmann Valves GmbH is gratefully acknowledged. Moreover, F. Taherkhani thanks E. Morales, M. Kollmeier, Z. Arabgol and B. Oswald from the HSU for technical support. The author also acknowledges the financial support by the federal ministry for economic affairs and climate action of Germany for funding of a ZIM-cooperation project under grant number of ZF4772101KO9.

Funding Open Access funding enabled and organized by Projekt DEAL.

References

1. D. Shrestha, F. Azarmi, and X. Tangpong, Effect of Heat Treatment on Residual Stress of Cold Sprayed Nickel-Based Superalloys, *J. Therm. Spray Technol.*, 2022, **31**, p 197-205. https://doi.org/10.1007/s11666-021-01284-x
2. K. Wu, W. Sun, A. Tan, E. Liu, and W. Zhou, An Investigation into Microstructure, Tribological and Mechanical Properties of Cold Sprayed Inconel 625 Coatings, *Surf. Coat. Technol.*, 2021, **424**, p 127660. https://doi.org/10.1016/j.surfcoat.2021.127660]
3. R.G. Neo, K. Wu, S.C. Tan, and W. Zhou, Effect of Spray Distance and Powder Feed Rate on Particle Velocity in Cold Spray Processes, *Metals*, 2022, **12**(1), p 75. https://doi.org/10.3390/met12010075
4. H. Zhou, C. Li, H. Yang, X. Lou, G. Yang, and W. Li, Pores Structure Change Induced by Heat Treatment in Cold-Sprayed Ti6Al4V Coating, *J. Therm. Spray Technol.*, 2019, **28**(6), p 1199-1211. https://doi.org/10.1007/s11666-019-00882-0
5. B. Yu, J. Tam, H.J. Cho, D. Poirier, G.D. Gianollardo, and U. Erb, Microstructural and Bulk Properties Evolution of Cold-sprayed Copper Coatings after Low Temperature Annealing, *Materialia*, 2019, **7**, p 100356. https://doi.org/10.1016/j.mtla.2019.100356
6. C. Huang, A. List, J. Shen, B. Fu, T. Chen, B. Klusemann, F. Gärtner, and T. Klassen, Tailoring Powder Strengths for Enhanced Quality of Cold Sprayed Al6061 Deposits, *Mater. Des.*, 2022, **215**, p 110494. https://doi.org/10.1016/j.matdes.2022.110494
7. Z. Zhang, D.H.L. Seng, M. Lin, S.L. Teo, T.L. Meng, C.J.J. Lee, Z. Zhang, T. Ba, and J. Guo, Cold Spray Deposition of Inconel 718 in Comparison with Atmospheric Plasma Spray Deposition, *Appl. Surf. Sci.*, 2021, **535**, p 147704. https://doi.org/10.1016/j.apsusc.2020.147704
8. P. Cavaliere, A. Rizzo, D. Valerini, and L. Capodieci, Wear and Fretting Behavior of Cold Sprayed IN625 Superalloy, *Metals*, 2020, **11**, p 49. https://doi.org/10.3390/met11010049
9. R. Vaßen, J. Fiebig, and T. Kalfhaus, Correlation of Microstructure and Properties of Cold Gas Sprayed Inconel 718 Coatings, *J. Therm. Spray Technol.*, 2020, **29**, p 1455-1465. https://doi.org/10.1007/s11666-020-00988-w
10. L.I. Pérez-Andrade, F. Gärtner, M. Villa-Vidaller, T. Klassen, J. Muñoz-Saldaña, and J.M. Alvarado-Orozco, Optimization of Inconel 718 Thick Deposits by Cold Spray Processing and Annealing, *Surf. Coat. Technol.*, 2019, **378**, p 124997. https://doi.org/10.1016/j.surfcoat.2019.124997
11. P. Cavaliere, A. Silvello, N. Cinca, H. Canales, S. Dosta, I. Garcia Cano, and J.M. Guilemany, Microstructural and Fatigue Behavior of Cold Sprayed Ni-based Superalloys Coatings, *Surf. Coat. Technol.*, 2017, **324**, p 390-402. https://doi.org/10.1016/j.surfcoat.2017.06.006
12. D. Srinivasan, V. Chandrasekhar, and R. Amuthan, Characterization of Cold-Sprayed IN625 and NiCr Coatings, *J. Therm. Spray Technol.*, 2016, **25**, p 725-744. https://doi.org/10.1007/s11666-016-0382-z
13. P. Poza, C.J. Múnez, M.A. Garrido-Maneiro, S. Vezzù, S. Rech, and A. Trentin, Mechanical Properties of Inconel 625 Cold-sprayed Coatings after Laser Remelting. Depth Sensing Indentation Analysis, *Surf. Coat. Technol.*, 2014, **243**, p 51-57. https://doi.org/10.1016/j.surfcoat.2012.03.018
14. A. Chaudhuri, Y. Raghupathy, D. Srinivasan, S. Suwas, and C. Srivastava, Microstructural Evolution of Cold-sprayed Inconel 625 Superalloy Coatings on Low Alloy Steel Substrate, *Acta Mater.*, 2017, **129**, p 11-25. https://doi.org/10.1016/j.actamat.2017.02.070
15. A. Klemm, F. Taherkhani, and M. Gündel, Additive Manufacturing of Steel Components by Cold Spraying, *CE/Papers*, 2023, **6**(3–4), p 739-744. https://doi.org/10.1002/cepa.2461
16. P. Kindermann, M. Strasser, and M. Wunderer, Cold Spray Forming: A Novel Approach in Cold Spray Additive Manufacturing of Complex Parts Using 3D-printed Polymer Molds, *Prog. Addit. Manuf.*, 2023 https://doi.org/10.1007/s40964-023-00521-9
17. I. Marinescu, Y. Huong, and E. Liu, Additive Manufacturing of Inconel625 Superalloy Parts Via High Pressure Cold Spray. *Proceedings of the 3rd International Conference on Progress in Additive Manufacturing (Pro-AM 2018), Singapore* (2018), p. 433-438
18. A. Sova, S. Grigoriev, A. Okunkova, and I. Smurov, Potential of Cold Gas Dynamic Spray as Additive Manufacturing Technology, *Int. J. Adv. Manuf. Technol.*, 2013, **69**, p 2269-2278. https://doi.org/10.1007/s00170-013-5166-8
19. P. Cavaliere and A. Silvello, Processing Parameters Affecting Cold Spay Coatings Performances, *Int. J. Adv. Manuf. Technol.*, 2014, **71**, p 263-277. https://doi.org/10.1007/s00170-013-5465-0
20. H. Assadi, T. Schmidt, and H. Richter, On Parameter Selection in Cold Spraying, *J. Therm. Spray Technol.*, 2011, **20**(6), p 1161-1176. https://doi.org/10.1007/s11666-011-9662-9
21. R. Rokni, S.R. Nutt, and C.A. Widener, Review of Relationship Between Particle Deformation, Coating Microstructure, and Properties in High-Pressure Cold Spray, *J. Therm. Spray Technol.*, 2017, **26**, p 1-48. https://doi.org/10.1007/s11666-017-0575-0
22. P. Cavaliere, A. Perrone, and A. Silvello, Fatigue Behavior of Inconel 625 Cold Spray Coatings, *Surf. Eng.*, 2018, **34**(5), p 380391. https://doi.org/10.1080/02670844.2017.1371872
23. F. Azarmi and I. Sevostianov, Comparative Micromechanical Analysis of Alloy 625 Coatings Deposited by Air Plasma

Spraying, Wire Arc Spraying, and Cold Spraying Technologies, *Mech. Mater.*, 2020, **144**, p 103345. https://doi.org/10.1016/j.mechmat.2020.103345
24. G.N. Devi, S. Kumar, T.S. Balaji, T.B. Mangalarapu, S.B. Chandrasekhar, A.V. Gopal, and A. Jyothirmayi, Influence of Inter-Splat Bonding State of Cold Sprayed IN625 and IN718 Coatings on Mechanical and Corrosion Performance, *Surf. Coat. Technol.*, 2022, **445**, p 128731. https://doi.org/10.1016/j.surfcoat.2022.128731
25. H. Assadi and F. Gärtner, Particle Compression Test: A Key Step Towards Tailoring of Feedstock Powder for Cold Spraying, *Coatings*, 2020, **10**(5), p 458. https://doi.org/10.3390/coatings10050458
26. T. Schmidt, H. Assadi, and F. Gärtner, From Particle Acceleration to Impact and Bonding in Cold Spraying, *J. Therm. Spray Technol.*, 2009, **18**, p 794-808. https://doi.org/10.1007/s11666-009-9357-7
27. www.matweb.com
28. D. Pereira, T. Clarke, and T. Hirch, Effect of Microstructure on Electrical Conductivity of Inconel 718 Alloys, *Mater. Sci. Technol.*, 2014, **31**, p 669-676. https://doi.org/10.1179/1743284714y.0000000638
29. F. Yong, L. Dong, and X. Hu, Effect of Solution Treatment Temperature Upon the Microstructure and Mechanical Properties of Hot Rolled Inconel 625 Alloy, *J. Mater. Sci.*, 2020, **55**, p 5613-5626. https://doi.org/10.1007/s10853-020-04375-2
30. R.A. Seraj, A. Abdollah-Zadeh, S. Dosta, H. Canales, H. Assadi, and I.G. Cano, The Effect of Traverse Speed on Deposition Efficiency of Cold Sprayed Stellite 21, *Surf. Coat. Technol.*, 2019, **366**, p 24-34. https://doi.org/10.1016/j.surfcoat.2019.03.012
31. H. Assadi, F. Gärtner, T. Stoltenhoff, and H. Kreye, Bonding Mechanism in Cold Gas Spraying, *Acta Mater.*, 2003, **51**(15), p 4379-4394. https://doi.org/10.1016/S1359-6454(03)00274-X
32. T. Schmidt, F. Gärtner, H. Assadi, and H. Kreye, Development of a Generalized Parameter Window for Cold Spray Deposition, *Acta Mater.*, 2005 https://doi.org/10.1016/j.actamat.2005.10.005
33. C. Borchers, T. Stoltenhoff, M. Hahn, M. Schulze, H. Assadi, C. Suryanarayana, and F. Gaertner, Strain-Induced Phase Transformation of MCrAlY, *Adv. Eng. Mater.*, 2015, **17**(5), p 723-731. https://doi.org/10.1002/adem.201400174
34. H. Assadi, H. Kreye, F. Gärtner, and T. Klassen, Cold Spraying-Cold Spraying–A Materials Perspective, *Acta Mater.*, 2016, **16**, p 382-407. https://doi.org/10.1016/j.actamat.2016.06.034
35. Z. Arabgol, M. Villa Vidaller, H. Assadi, F. Gärtner, and T. Klassen, Influence of Thermal Properties and Temperature of Substrate on the Quality of Cold-sprayed Deposits, *Acta Mater.*, 2017, **127**, p 287-301. https://doi.org/10.1016/j.actamat.2017.01.040
36. Z. Arabgol, H. Assadi, and T. Schmidt, Analysis of Thermal History and Residual Stress in Cold-Sprayed Coatings, *J. Therm. Spray Technol.*, 2014, **23**, p 84-90. https://doi.org/10.1007/s11666-013-9976-x
37. S. Bagherifard, I. Fernàndez Parienete, R. Ghelichi, M. Guagliano, and S. Vezzù, Effect of Shot Peening on Residual Stresses and Surface Work-Hardening in Cold Sprayed Coatings, *Key Eng. Mater.*, 2010, **417–418**, p 397-400. https://doi.org/10.4028/www.scientific.net/KEM.417-418.397
38. W. Sun, A. Tan, K. Wu, S. Yin, X. Yang, I. Marinescu, and E. Liu, Post-Process Treatments on Supersonic Cold Sprayed Coatings: A Review, *Coatings*, 2020, **10**(2), p 1-35. https://doi.org/10.3390/coatings10020123